CrystEngComm

Accepted Manuscript

This article can be cited before page numbers have been issued, to do this please use: E. Podda, M. Arca, A. Pintus, V. Lippolis, C. Caltagirone, S. Coles, J. B. Orton, G. Ennas, G. Picci, R. Davies and M. C. Aragoni, *CrystEngComm*, 2023, DOI: 10.1039/D2CE01552H.

ROYAL SOCIETY OF CHEMISTRY

rsc.li/crystengcomm

View Article Online
DOI: 10.1039/D2CE01552H

ARTICLE

On the role of torsional dynamics in the solid-state fluorescent properties of a new bifluorene-tetracarboxylic acid and its supramolecular assemblies: a structural and TD-DFT investigation†

Received 00th January 20xx,
Accepted 00th January 20xx

DOI: 10.1039/x0xx00000x

Enrico Podda,[a,b] Massimiliano Arca,[a] Anna Pintus,[a] Vito Lippolis,[a] Claudia Caltagirone,[a] Simon J. Coles,[d] James B. Orton,[d] Guido Ennas,[a] Giacomo Picci,[a] Robert P. Davies,*[c] M. Carla Aragoni*[a]

The novel butterfly-shaped tetracarboxylic acid [9,9'-methylene-bis(9-methylfluorene-2,7-dicarboxylic acid), H_4L] featuring a co-facial bifluorene core was designed and synthesised. Reactions of H_4L with Cd^{II} produced the luminescent supramolecular frameworks 2 and 3, with different dimensionality and wingspan of L^{4-}. The solid-state emission properties were rationalised based on the torsional dynamics of the facing bifluorene units by means of X-ray diffraction analysis and TD-DFT calculations.

Introduction

Fluorene derivatives have been extensively studied during the past years for their versatile role in material science, and particular interest has been devoted to polyfluorenes due to their electroactive and photoactive nature that allows for the preparation of blue-light emitting diodes with tuneable electronic and emission properties.[1–6] Oligo- and poly-fluorenes were employed as models in the design of functional polymeric materials for the understanding of excimer formation and hole-stabilization in π-stacked assemblies.[7–12] Supramolecular constructs originating from the interaction of fluorene derivatives and metal ions were prepared giving rise to coordination polymers (CPs) and metal-organic frameworks (MOFs) featuring remarkable properties allowing for their applications as separating agents,[13–15] sensors[16–18] and electro-phosphorescent materials.[19] The key role of fluorene derivatives in the preparation of sensing materials lies in the variation of their photoluminescent response according to the nature of the interacting guests. The role of poly-fluorenes as supramolecular synthons is still largely untapped, and all the above-cited examples include either single fluorene or spiro-bifluorene derivatives.[20,21] Belonging to the above-mentioned class of poly-fluorenes derivatives, cofacial bifluorenes can provide additional advantages when applied to crystal engineering, since the overlapping extent of the facing fluorene units may potentially lead to variations in the fluorescent response. The chemical and geometrical features of the substituents introduced in the fluorene rings influence in turn the face-overlapping and the resulting emission properties of the material.[7] Moreover, the interaction with metal nodes in the self-assembly could itself affect the geometry adopted by the organic linkers leading to unprecedented architectures and modulated fluorescence properties. Therefore, we designed the brand new co-facial bifluorene-based linker 9,9'-methylene-bis(9-methylfluorene-2,7-dicarboxylic acid), H_4**L**, as a tecton for the assembly of fluorescent supramolecular networks. The unprecedent design of H_4**L** with four carboxylic acid groups distributed on two methylene-bridged fluorene units opens new perspectives in the preparation of robust and optically active porous materials based on polycarboxylic acids.[22]

Results and Discussion

Synthesis and Structural Characterization

The precursors **1b** and **1c** were prepared starting from commercial **1a**, as previously described.[7] The linker H_4**L** was prepared according to the synthetic route outlined in Scheme 1 by adapting a procedure we previously reported for the synthesis of siloxane-based linkers.[23]

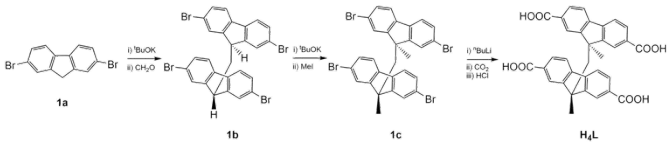

Scheme 1 Synthetic steps leading to H_4**L** starting from compound **1a**.

The tetrabrominated compound **1c** and the linker H_4**L** were structurally characterized by means of single crystal X-ray diffraction (XRD) analysis (Tables S1 and S4†).‡ Compound **1c** crystallises in the monoclinic space group $P2_1/c$ with a single molecule in the asymmetric unit (Fig. S1†). The two fluorene

a. Dipartimento di Scienze Chimiche e Geologiche, Università degli Studi di Cagliari, Cittadella Universitaria, SS. 554 bivio Sestu, 09042 Monserrato – Cagliari, Italy.
b. Centro Servizi di Ateneo per la Ricerca, Università degli Studi di Cagliari, Cittadella Universitaria, SS. 554 bivio Sestu, 09042 Monserrato – Cagliari, Italy.
c. Department of Chemistry, Imperial College London, White City Campus, 80 Wood Lane, London W12 0BZ, United Kingdom.
d. UK National Crystallography Service, School of Chemistry, Faculty of Engineering and Physical Sciences, University of Southampton, SO17 1BJ, United Kingdom.

† Electronic Supplementary Information (ESI) available: spectroscopic characterizations: FT-IR, solution and solid-state absorption and emission, NMR, SC-XRD, PXRD, DSC, and DFT calculations. See DOI: 10.1039/x0xx00000x

View Article Online
DOI: 10.1039/D2CE01552H

units are almost co-facial with an angle α = 14° between the planes of the fluorene moieties and a dihedral angle τ = 25° calculated along the torsional coordinate *via* methylene linkers, in a "closed wings" configuration (see Fig. 1 for α and τ definition).

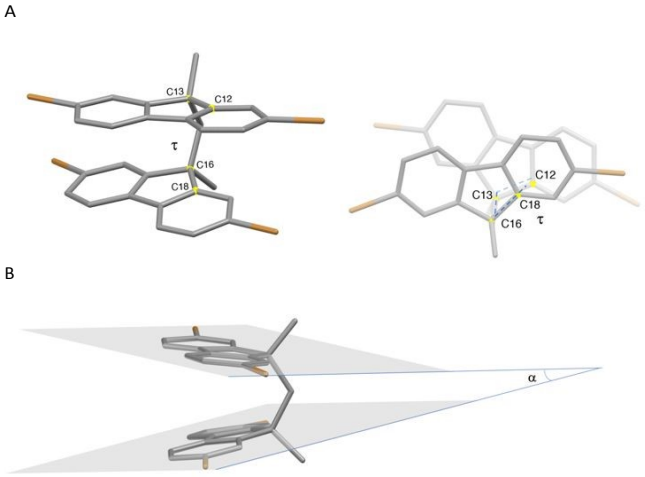

Fig. 1 Crystal structure of **1c**: angle α (A) and torsion angle τ (C12-C13-C16-C18, B) parameters.

The outer rings of both fluorene units show intra- and inter-molecular π-π interactions with centroid distances of 3.63, and 3.73 Å, respectively, leading to face-to-face dimeric constructs packed along the *a* axis through Br···Br weak contacts in a herringbone pattern leading to a 2D network (Figs. S2 and S3[†]).

The tetracarboxylic acid H_4**L** crystallises in the triclinic space group *P*-1 with one molecule in the asymmetric unit (Fig. 2A).

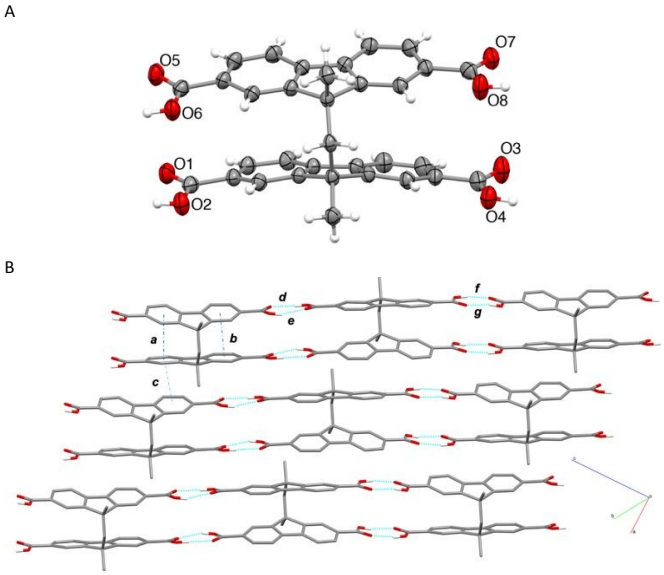

Fig. 2 (A) Asymmetric unit of H_4**L**. Thermal ellipsoids were drawn at 50 % probability level. (B) Packing view of the 1D hydrogen-bonded chains; intramolecular and intermolecular π-π centroid distances: ***a*** = 3.47, ***b*** = 3.66, ***c*** = 3.89 Å; HBs: ***d***: O6^{i}–H6^{i}···O1 2.641(3), 1.79(6), 175(5); ***e***: O2–H2···O5^{i} 2.604(3), 1.82(2), 160.3(2); ***f***: O8^{ii}–H8^{ii}···O3 2.589(3),1.75(5),170(6); ***g***: O4–H4···O7^{ii} 2.664(3) Å,1.84(6) Å, 171(6)°. Hydrogen atoms were omitted for clarity except for those involved in HBs. Symmetry: ^{i} = 1–*x*, –*y*, –*z*; ^{ii} = 1–*x*, 2–*y*, 1–*z*.

The butterfly-shaped compound features an opening angle α = 20° wider than that found for **1c**.

The compound H_4**L** features four carboxylic groups, located at the 2 and 7 positions of each fluorene moiety, almost coplanar to the respective fluorene moieties [torsion angles in the range 5.8(5)–13.7(3)°]. The HBs involving the carboxylic groups of both fluorene moieties induce a dramatic decrease of τ angle (τ = 5°) and a larger overlap between the cofacial fluorene units, that results in intramolecular (**a** and **b** in Fig. 2B) and intermolecular (**c** in Fig. 2B) π-π interactions featuring centroid distances of 3.47, 3.66, and 3.89 Å that stack the chains in 2D layers (Fig. 2B). The layers interact by means of weak HBs in an overall 3D network (Fig. S4[†] in ESI).

Upon deprotonation, the four carboxylic groups are potentially available for metal coordination. H_4**L** was therefore reacted with $Cd(NO_3)_2{\cdot}4H_2O$ in a 1:2 molar ratio in dimethylacetamide (DMA)/H_2O mixture (2:1 *v*/*v*) at 90 °C for 24 h. The reaction yielded colourless crystals characterized by single-crystal XRD as the CP $[Cd_2\mathbf{L}(H_2O)_6{\cdot}2H_2O]_\infty$ (**2**). Compound **2** crystallised in the triclinic space group *P*-1 with a single $\mathbf{L}^{4-}$ unit, two Cd^{II} ions, six coordinated and two co-crystallised water molecules in the asymmetric unit (Fig. 3A, Table S2[†]).

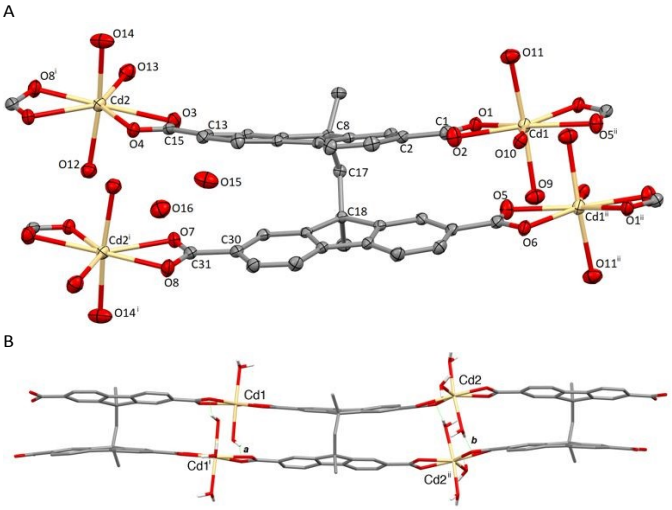

Fig.3 Crystal structure of CP **2**: (A) View of **2** with atom labelling scheme, ellipsoids at 50% probability level (H atoms omitted for clarity). (B) View of the coordination polymer (only H atoms of the water molecules are shown). HBs: ***a***: O$_9$–H$_{9A}$···O$_6$ 2.759(4), 1.97(3), 152.2(2); ***b***: O$_{12}$–H$_{12A}$···O$_4^{i}$ 2.693(4) Å, 1.85(3) Å, 174.2(2)°. Symmetry: ^{i} = –*x*, –*y*, 1–*z*; ^{ii} = 1–*x*, 2–*y*, –*z*.

Both Cd^{II} ions are hepta-coordinated in a pentagonal-bipyramidal geometry: the five equatorial positions are occupied by two chelating carboxylates and one water molecule; two axially bound water molecules complete the coordination sphere around the metal ions (Fig. 3A).

The tetracarboxylate bifluorene unit features α and τ angles of 19° and 25°, respectively, and intramolecular centroid distances of 3.77 and 3.70 Å, slightly longer than those found in H_4**L**, due to the increased displacement between the facing bifluorene planes. The $\mathbf{L}^{4-}$ spacers bridge couples of symmetry-related Cd1 and Cd2 ions through the four carboxylate anions giving rise to infinite ribbons (Fig. 3B). The ribbons pack through strong HB interactions involving the carboxylate oxygen atoms and both

coordinated and co-crystallised water molecules (Figs S5-S6† and Table S5† in ESI†).

The 1:2 molar ratio reaction between H_4**L** and $Cd(NO_3)_2{\cdot}4H_2O$ in the same DMA/H_2O (2:1 *v*/*v*) mixture was also performed at 120 °C affording crystals of two different morphologies derived via the concurrent formation of the previously described CP **2**, and a 3D-MOF with formula $[Cd_2\mathbf{L}(H_2O)_3{\cdot}3H_2O]_\infty$ (**3**).†‡ Compound **3** crystallised in the orthorhombic non-centrosymmetric space group *Cmc*2_1. The asymmetric unit comprises halves of four crystallographically independent Cd^{II} ions, a fully deprotonated $\mathbf{L}^{4-}$ ligand and five coordinated water molecules, four of which lie on special positions (Fig. 4A, Table S3†).§ The linker shows angles α and τ of 7 and 22° with intramolecular centroid distances of 3.56, 3.24 and 3.62 Å.

The four carboxylate groups of $\mathbf{L}^{4-}$ coordinate four independent cadmium ions adopting three different coordination modes (see Scheme S1†): I) chelating; II) chelating/bridging; III) bridging. The detailed description of the different coordination geometries around each cadmium ion is shown in Fig. 4B.

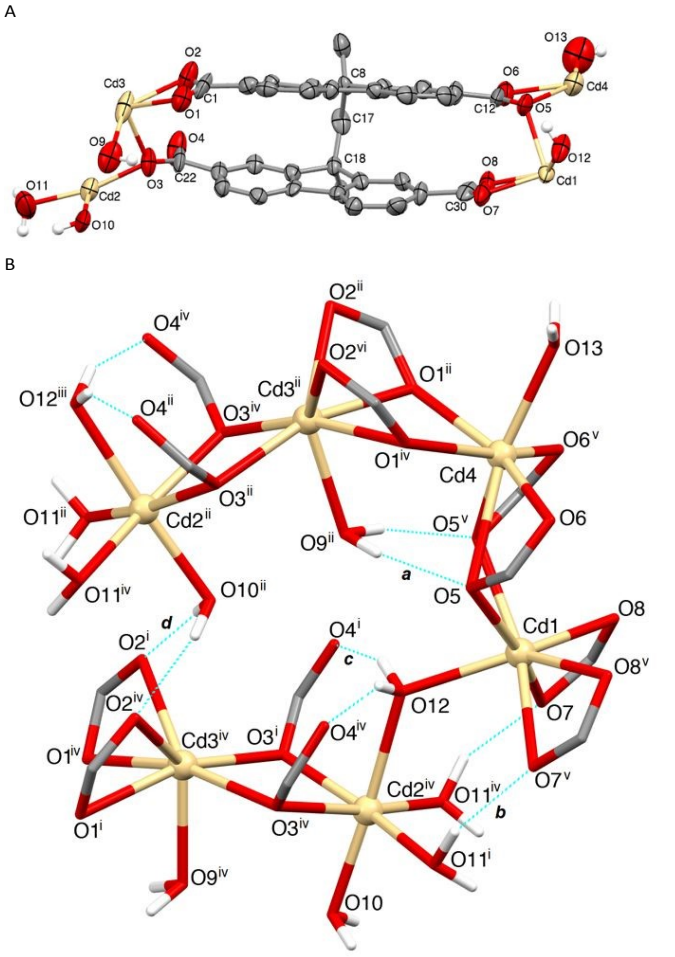

Fig. 4 Crystal structure of the MOF **3**: (A) asymmetric unit. (B) Cd coordination environments. Interactions are summarised in Table S6†. [i] = 3/2–x, 1/2+y, z; [ii] = 3/2–x, 3/2–y, –1/2+z; [iii] = 2–x, 2–y, –1/2+z; [iv] 3/2–x, 1/2+y, z; [v] = 2–x, y, z; [vi] = 1/2+x, 3/2–y, –1/2+z.

Cd1, Cd3 and Cd4 are hepta-coordinated and adopt a capped trigonal prismatic geometry constructed by six differently coordinated symmetry related carboxylates and one capping H_2O molecule. The Cd2 ion is hexa-coordinated into a distorted octahedral geometry by two μ_2-oxygens from two different $\mathbf{L}^{4-}$ anions and four water molecules (Fig. 4B and Table S6†). The described coordination environments generate a MOF with S-shaped (sinusoidal) secondary building units (SBUs) formed by edge-shared Cd-polyhedra of different shapes (Fig. 5A).[24] The overall three-dimensional MOF **3** shown in Fig. 5B is characterized by ellipsoidal channels with openings of approximatively 8.5 x 3 $Å^2$ that occupy 17% of the unit cell volume.

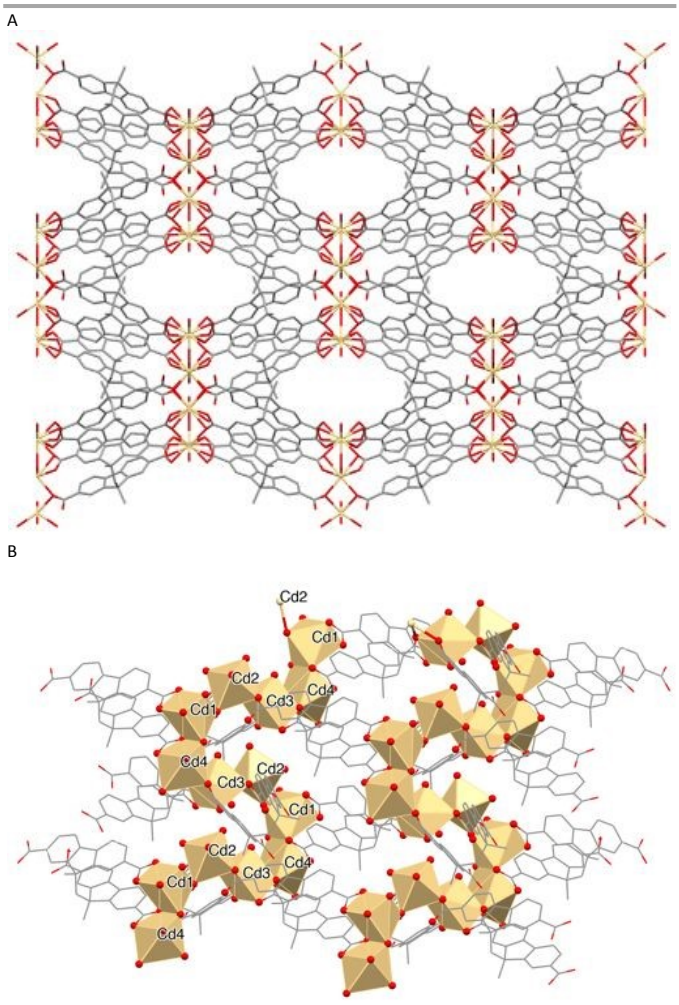

Fig. 5 (A) (C) Packing view of the infinite Cd arrangement. (B) Packing diagram along the *c* axis.

Three disordered water molecules are present in the asymmetric unit and were subjected to the SQUEEZE routine.§ Unfortunately, since compound **3** was not obtained pure, stability on evacuation, porosity measurements, and gas sorption studies were not carried out.

Powder XRD measurements were carried out on the solid-state products obtained by different reactions of H_4**L** and $Cd(NO_3)_2{\cdot}4H_2O$ performed in different experimental conditions. The experimental results, compared with the simulated patterns calculated from the single crystal XRD data of CP **2** and MOF **3** (Fig. S7†), show that, depending on the reaction temperature, either the pure CP **2** (90 °C) or a mixture of **2** and **3** (120 °C) are formed (named **2+3** in the following). All attempts

to obtain a bulk sample of pure **3** failed. TGA analyses performed on **2** and **2+3** show that both samples have a significant weight loss in the range 120-170° C suggesting a decomposition of both compound **2** and the mixture **2+3**. Accordingly, the DSC measurements show endothermic processes in the same temperature range (Fig. S8†).

Photophysical Measurements

The absorption and emission spectra of the synthesised compounds were recorded both in solution and in the solid state for H_4**L**, and in the solid state for **2** and the mixture **2+3**, whilst no emission was observed for **1c**. In DMSO solution, H_4**L** featured a structured absorption band at about 310 nm. A similar spectral shape could be seen in the diffuse reflectance spectrum, showing a broad absorption in the range 300–380 nm, with a maximum at about 335 nm (Fig. S9†). Compound **2** and the mixture **2+3** display diffuse reflectance spectra very similar to that of H_4**L** (Fig. S10†).

Excitation at 303 and 372 nm led to strong fluorescent emission bands at 436 and 491 nm in DMSO solution and in the solid-state, respectively, for H_4**L** (Fig. S9†). Therefore, in the solid state both the absorption and emission energies are bathochromically shifted as compared to those recorded in DMSO solution. A comparison with the solid-state emission properties for the mono-fluorene derivative 9,9'-dimethylfluorene-2,7-dicarboxylic acid,[25] reported at 410 nm, evidences a significative difference in the emission wavelength on passing from the mono- to the bi-fluorene derivative, tentatively ascribable to the co-facial arrangement of the fluorene units (τ = 5°). A comparison of the normalized emission spectra of H_4**L**, **2** and **2+3** (Fig. 6) shows a shift of the emission band to 433 nm for both cadmium supramolecular constructs **2** and **2+3**.

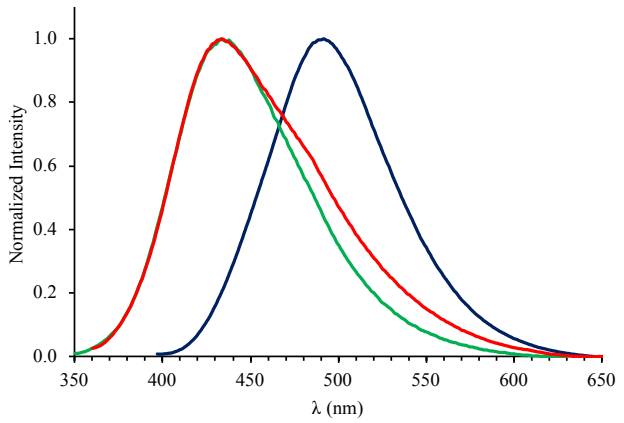

Fig. 6 Normalised solid-state emission spectra determined for H_4**L** (blue), **2** (green) and the mixture **2+3** (red). λ_{ex} = 372, 330, and 340 nm for H_4**L**, **2**, and **2+3**, respectively.

It is worth pointing out that differences of only 5 nm in the solid-state emission wavelengths were evidenced on passing from the above mentioned 9,9'-dimethylfluorene-2,7-dicarboxylic acid to the corresponding zinc and cadmium supramolecular constructs.[25] The significant variation observed in the case of our systems can be tentatively explained by taking into account the increased displacement between the facing fluorene planes found in cadmium supramolecular constructs as compared to free H_4**L** (τ = 5, 25 and 22° for H_4**L**, **2** and **3**, respectively, see above).

TD-DFT Calculations

The absorption and emission properties of H_4**L** were elucidated by means of DFT[26] and TD-DFT calculations (PBE0//def2-SVP; see Experimental section and Tables S7–S9†)[27, 28] carried out in the gas phase and in DMSO by using the polarizable continuum self-consistent reaction field model in its integral-equation formalism (SCRF IEF-PCM).[29] Notably, in the gas phase the four carboxylic groups show orientations very close to those determined by XRD, with torsion angle with respect to the relevant fluorene moieties in the range 2.7–10.5°. The torsion angle between the two fluorine units calculated at the optimised geometry for H_4**L** is τ = 26.0°, i.e. very similar to the structural value of **1c**. This similarity suggests that the crystal-packing interactions, and in particular the strong HBs involving the carboxylic acids, could be responsible for the small τ value of the facing fluorene units found in the crystal structure of H_4**L**,

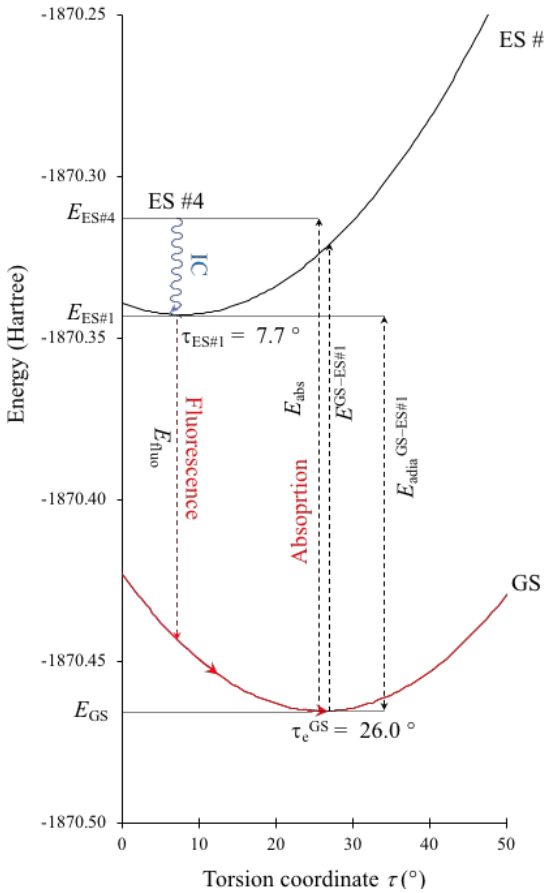

Fig. 7 Quantitative energy diagram for the absorption and emission processes calculated for H_4**L**. The energies of the GS (red curve) and the ES #1 (black line) are depicted as a function of the torsion angle τ. E_{GS} and E_{ES} are the minimum energies of the ground state and excited states, respectively (neglecting ZPE corrections). Arrows schematically represent the excitation and relaxation paths.

which was proved to be directly related to the energies of the ground (GS) and excited states (ES) involved in the absorption and emission processes calculated for H_4**L**. In Fig. 7 a quantitative Jablonsky diagram for the singlet states calculated for H_4**L** at the optimised geometry is depicted.

The allowed vertical transition lying at the lowest energy (GS→ES #4) is calculated for H_4**L** at E_{abs} = 4.162 eV (corresponding to λ_{abs} = 297.9 nm) in the gas phase. In DMSO, the corresponding excitation involves the GS→ES #3 transition (E_{abs} = 4.089 eV, λ_{abs} = 303.2 nm) in excellent agreement with the experimental value (λ_{abs} = 310 nm, see above). These transitions are assigned to Kohn-Sham (KS) HOMO-1→KS-LUMO+1 and KS-HOMO→KS-LUMO one-electron π–π* excitations [see Fig. S11† and Table 1; natural transition orbitals (NTOs)[30] involved in the GS→ES #4 transition are depicted in Fig. S12†), i.e. involve MOs delocalised on both fluorene units of H_4**L**. To investigate the emission properties of H_4**L**, the geometry of ES #1 was optimised, and the emission energy E_{fluo} and wavelength λ_{fluo} were calculated (see ESI for details; λ_{fluo} = 450.2 and 468.2 nm in the gas phase and DMSO solution, respectively, Table S8†). According to Kasha's rule,[31] after internal conversion ES #4→ES #1 and vibrational relaxation of the first excited state, luminescent emission occurs from ES #1 to GS.

Table 1. Energy E_{abs} (eV) calculated for singlet-singlet electronic transitions, corresponding wavelengths λ_{abs} (nm), oscillator strengths *f* and main contributing mono-electronic excitations for the four lowest excited states calculated on H_4**L** in the gas phase and DMSO at TD-DFT level.

	Gas phase				DMSO			
Exc. State	#1	#2	#3	#4	#1	#2	#3	#4
E_{abs}	3.869	3.917	3.974	4.162	3.727	3.920	4.089	4.093
λ_{abs}	320.5	316.6	312.0	297.9	332.7	316.3	303.2	302.9
f	0.009	0.014	0.025	0.842	0.014	0.032	1.257	0.016
Excitations[a]	143→144 (93%)	142→144 (41%) 143→145 (58%)	142→145 (94%)	142→144 (54%) 143→145 (36%)	143→144 (98%)	142→144 (35%) 143→145 (63%)	142→144 (62%) 143→145 (32%)	142→145 (99%)

[a] KS-HOMO = MO 143.

The most remarkable difference between the metric parameters optimised for the GS and ES #1 involves the τ angle (Fig. 1; τ = 26.0 and 7.7° for GS and ES#1, respectively in the gas phase; τ = 21.6 and 2.3° for GS and ES #1, respectively in DMSO), indicating that vibrational relaxation processes result in a variation of the relative orientation of the two fluorene units. After the emission due to the radiative relaxation ES #1→GS, the GS undergoes a vibrational thermalization to the equilibrium geometry. As previously observed, the XRD analysis showed that in the solid state H_4**L** is locked in a cofacial conformation of the two fluorene moieties with a τ angle (5°) that is very close to that optimised for the ES #1 (7.7°), thus possibly accounting for the difference in the transition energies determined in the solid state with respect to the corresponding values recorded in DMSO (see above).

DFT calculations were extended to the $[Cd_4\mathbf{L}_2(H_2O)_{16}]$ model complex (**4**, Fig. S13†), mimicking a portion of the CP **2**. In complex **4**, the $\mathbf{L}^{4-}$ anion bridges four Cd^{II} metal ions by means of the four carboxylate groups, the water molecules completing a distorted octahedral coordination at each metal ion. Notably, the frontier KS-MOs calculated for complex **4** at the optimised geometry (τ = 24.43°) are π-in-nature MOs exclusively localized on the aromatic portion of the bifluorene moieties of the $\mathbf{L}^{4-}$ anion (Fig. S13†). Accordingly, excitation processes are completely ligand-centred and occur at energy values very similar to that calculated for H_4**L**. In fact, the first allowed electronic absorption at the lowest energy involves the transition from the GS to the ES #4 ($E^{GS-ES\#4}$ = 3.941 eV; $l^{GS-ES\#4}$ = 314.6 nm; *f* = 0.959; Table S9†) and is mainly due to the KS-HOMO–1→LUMO and HOMO→LUMO+1 monoelectronic excitations (main NTOs involved in the GS→ES #4 transition are depicted in Fig. S14†). Finally, neglecting the vibrational relaxation of ES #1 of H_4**L** and **4**, the lowest energy of the GS→ES #1 transition calculated **4** with respect to H_4**L** might account for the blu-shift of **2** and **2+3** mixture as compared to the starting ligand H_4**L** (Fig. 6).

Conclusion

The results reported on the new bifluorene-tetracarboxylate 9,9'-methylene-bis(9-methylfluorene-2,7-dicarboxylic acid) (H_4**L**) and its CP (**2**) and MOF (**3**) assemblies show the potential of the spacer in the realm of supramolecular chemistry due to its structural features, intrinsic fluorescence and of the possibility of varying the emission properties either by changing the carboxylate coordination environments or by acting on its geometrical features.

Summarily, the peculiar solid-state cofacial constrained conformation of H_4**L** (absent in DMSO solution), can be considered responsible for its emission at higher energy as compared to mono-fluorene derivatives and to the Cd^{II} complexes **2** and **3**. This suggests not only that the emission energies of bifluorene derivatives can be fine-tuned by structural modifications affecting their rigidity, but also that subtle structural modifications, such as the introduction of terminal carboxylates, can be fundamental in determining the resulting emission energies.

The presented ligand can be thus considered the first precursor of a novel family of π-stacked carboxylate synthons to be used in crystal engineering suitable for sensing applications. Further work is being conducted in our labs at both the theoretical and experimental level to study the reactivity of H_4**L** and structurally related ligands with different cations and anions in solution and in the solid state.

Experimental

Materials

All chemicals, reagents, and solvents were purchased from Sigma Aldrich, TCI, Fluorochem, or VWR Chemicals and used as received without any further purification if not otherwise stated.

Spectroscopic Characterisation

FT-Infrared spectra were recorded on a Thermo Nicolet 5700 spectrometer on KBr pellets.

Mass spectra were recorded on a Waters LCT Premier (ES-ToF)/Acquity i-Class spectrometer.

NMR measurements were performed on a Bruker Avance III HD 400 MHz spectrometer. The chemical shifts (δ) are reported in ppm and referenced against the solvent residue. UV-Vis measurements in solution were recorded in the range 190-1100 nm using quartz cuvettes with a path length of 1 cm by means of an Agilent Cary 5000 UV−vis−NIR dual-beam spectrophotometer.

Diffuse reflectance measurements were carried out on an Agilent Cary 5000 UV−vis−NIR dual-beam spectrophotometer equipped with a diffuse reflectance accessory. Photoluminescence emission spectra in solution and in the solid-state were collected either on a Varian Cary Eclipse spectrofluorometer or a Perkin Elmer LS55 fluorescence spectrometer.

DSC and TGA Measurements

Thermogravimetric analysis (TGA) and differential scanning calorimetry analysis (DSC) were performed on Perkin-Elmer series 7 thermal analyzers in a temperature range between 100 and 400 °C (20 °C min-1) under nitrogen flow (40 mL min^{-1}).

X-Ray Diffraction

Single-Crystal X-ray diffraction data of H_4**L** and **3** with CuK_α radiation, on a Rigaku 007HF diffractometer, equipped with Varimax confocal mirrors, an AFC11 goniometer, a HyPix 6000 detector, and an Oxford Cryosystems low-temperature device, operating at 100 K. The diffractometric data for compounds **1c** and **2** were collected with MoK_α radiation, on a Rigaku FRE+ diffractometer, equipped with HF Varimax confocal mirrors, an AFC12 goniometer, a HyPix 6000 detector, and an Oxford Cryosystems low-temperature device, operating at 100K. Data collection and processing were performed using CrysAlisPro (Rigaku Oxford Diffraction).[32] The structures were then solved with ShelXT[33] structure solution program (using the Intrinsic Phasing solution method), and by using Olex2[34] as the graphical interface with their models refined with version 2018/3 of ShelXL,[35] using Least Squares minimization.

Powder X-ray Diffraction analyses were performed on a Bruker D8 Advance equipped with CuK_α radiation and LYNXEYE detector in 1D mode. The scan step was set to 0.05° and a scan speed of 0.5 s/step in the range from 4 to 30° (2Θ). Experimental patterns were then compared with those calculated from single-crystal X-ray diffraction analysis by means of DIFFRACT.EVA.

TD-DFT Calculations

Theoretical calculations were carried out at the density functional theory (DFT)[26] level by using the Gaussian 16[36] commercial suite of computational software on H_4**L** by adopting the PBE0[27] hybrid functional paralleled by different basis sets, namely 6-31G, 6-311G, 6-311+G(d,p)[37] and Ahlrichs split-valence double-ζ plus polarization (pVDZ) sets, both in their original form[38] and in Weigend's[28] recent formulation (def2-SVP), and the corresponding triple-ζ plus polarization def2-TZVP.[39] Notwithstanding numerous attempts, including the variation of the SCF convergence algorithm and the energy optimization threshold, the optimization of the excited state (ES) #1 was unsuccessful with the largest basis sets. The validation of the computational setup was carried out by comparing the results from TD-DFT calculations with the experimental values, in particular the absorption and the emission wavelengths (λ_{abs} and λ_{em}, respectively) for H_4**L**. Among the remaining basis sets, absorption and emission energies were calculated both in the gas phase and in DMSO solution, solvation being implicitly considered by means of the polarizable continuum SCRF model in its integral equation formalism (IEF-PCM), describing the cavity of the complexes within the reaction field (SCRF) through a set of overlapping spheres.[29] Very similar results were obtained (with τ angles varying within 1.5° and absorption energies within 0.07 eV), with an optimal balance between the reliability of the calculated parameters and the computational costs obtained with the def2-SVP basis set (Table S7† in ESI).

Finally, the results achieved with the PBE0 functional were compared with those obtained with the hybrid exchange–correlation functional using the Coulomb-attenuating method CAM-B3LYP,[40] including long-range corrections.[41] Unfortunately, this functional largely overestimated both absorption and emission energies and was eventually discharged (CAM-B3LYP/def2SVP: gas phase, λ_{abs} = 279.2 nm, λ_{em} = 393.0 nm; DMSO λ_{abs} = 284.1 nm, λ_{em} = 406.2 nm). The effect of the mutual orientation of the carboxylic groups was investigated by optimizing separately H_4**L** not only in the structural conformation, showing the OH groups disposed one above the other, but also in the alternate disposition. The energy difference between the two isomers was found to be negligible (differing from the former by $4.94 \cdot 10^{-4}$ Hartree (corresponding to 0.31 kcal mol^{-1}). Calculations were extended to complex **4** at the same PBE0//def2-SVP theoretical level. For all compounds, tight SCF convergence criteria and fine numerical integration grids were used. Optimized geometries were verified by harmonic frequency calculations, including the determination of thermochemistry parameters (zero-point energy ZPE corrections and thermal corrections to enthalpy and Gibbs free energy) and the calculation of FT-Raman frequencies. A complete natural population analysis (NPA) was carried out with a natural bonding orbital (NBO)[42] partitioning scheme to investigate the charge distributions. Absorption vertical transition energies, wavelengths, and oscillator strengths were calculated at the time-dependent (TD) DFT level, by evaluating the lowest ten excited states. The calculation of absorption and emission energies was carried out as outlined previously.[43, 44] The frontier Kohn-Sham molecular orbitals involved in the electronic absorption at the lowest energies are depicted in Fig. S11† for H_4**L** and Fig. S13† for the model complex **4**. The absorption maximum at the lowest energy was calculated at TD-DFT level by considering the lowest vertical transition with non-negligible oscillator strength (GS→ES #4). The natural transition orbitals (NTOs)[30] with the largest occupation for the transition GS→ES #4 in the gas phase are depicted in Fig. S12† and Fig. S14† for H_4**L** and the complex **4**, respectively.

Emission energies were calculated for H_4**L** by evaluating the GS→ES #1 energy at the geometry optimized for ES #1. Although any attempts to optimize ES #4 did not achieve an acceptable SCF convergence, the geometry of ES #1 in the gas phase converged to τ = 35.3°, thus suggesting the hypothesis that a direct crossing of ES #4 and ES #1 may occur at about τ =

30°. The energy curves in Fig. 7 were calculated by adapting a Morse-type equation to the electronic energy *E* as a function of τ:

$$E = E_e \cdot \{[1 - e^{a(\tau - \tau_e)}]^2\}$$

where, for each electronic state (GS or ES), E_e represents the energy of the relevant minimum, τ_e the equilibrium (optimized) torsion value, and a is defined as:

$$a = \sqrt{\frac{k}{2|E_e|}}$$

with k being the force constant at the minimum energy value and being fitted with the calculated E_{abs} and E_{fluo} values (Table 1 and Table S8[+]; $|a|$ = 1.826·10^{-4} and 2.206·10^{-4} for the GS and ES #1, respectively). Solvation in absorption/emission processes was calculated within a non-equilibrium approach, by neglecting solvent molecular motion in the timescale of absorption and fluorescence processes.

Molden 6.2[45] and GaussView 6.0.16[46] were used to analyze Kohn−Sham (KS) molecular orbital (MO) compositions and energies. Chemissian 4.54[47] was used to evaluate the atomic orbital contributions to KS-MOs and to analyse the contribution of one-electron excitations to molecular transitions. All calculations were carried out on the CINECA Galileo100 supercomputer.

Synthesis

Compounds **1a**–**1c** were prepared as previously described.[7]

*Synthesis of 9,9'-methylene-bis(9-methylfluorene-2,7-dicarboxylic acid) (H$_4$**L**):* in a 100 mL two-necked round bottom flask 40 mL of dry THF were cooled at -78 °C and then 2.4 mL of n-BuLi (2.5 M in hexane) were added under N_2 atmosphere. After stirring for 15 min at the same temperature, a solution of **1c** (1.00 g; 1.45 mmol) in dry THF (20 mL) was added dropwise to the first solution and the resulting mixture was stirred for 1.5 h. CO_2 was then bubbled into the reaction mixture for 3 h, resulting in a colour change from pink to purple. The reaction mixture was then kept under N_2 atmosphere overnight and the temperature slowly raised to room temperature. An aqueous 1 M HCl solution (30 mL) was added to quench the reaction, resulting in the precipitation of the product which was collected by filtration, washed with water and ethyl acetate, and dried under vacuum (560 mg; 1.02 mmol; 70%). FT-IR (KBr 400-4000 cm^{-1}): 3437w, 2964br, 2594br, 1689vs, 1608s, 1585s, 1491w, 1469m, 1450ms, 1413s, 1302vs, 1259vs, 1115m, 1007w, 918m, 905m, 835m, 762s, 663m, 580w, 515m, 509m, 428m cm^{-1}. ^{1}H NMR (400 MHz, DMSO-d_6) δ 12.60 (br, 4H, OH), 7.61 – 7.47 (m, 8H), 7.30 – 7.19 (m, 4H), 3.31 (s, CH_2), 1.33 (s, 6H, CH_3) ppm (Fig. S13). ^{13}C{^{1}H} NMR (101 MHz, DMSO-d_6) δ 167.0, 150.5, 141.9, 129.4, 127.7, 124.7, 119.7, 49.3, 40.2, 28.6 ppm (Fig. S14). ^{1}H-^{13}C HMQC of H$_4$**L** in DMSO-d_6 Fig. S15. (TOF MS ES-) for (M-H)$^-$ $C_{33}H_{23}O_8^-$ (m/z): calcd 547.1393; found 547.1406 (Fig. S16). Φ (DMF, quinine sulfate) = 0.209.

*Synthesis of **2**:* an 8 mL glass vial was loaded with 6 mL of a DMA/H_2O mixture (2:1 v/v), a solution of H$_4$**L** in DMA (200 µL, 0.25 M), and an aqueous solution of $Cd(NO_3)_2{\cdot}4H_2O$ (400 µL, 0.25 M). The mixture was sonicated for a few minutes and then heated to 90 °C for 24 h. The mixture was then cooled to room temperature at a rate of 10 °C/h. Colorless crystals were isolated and structurally characterized.

*Synthesis of mixture **2+3**:* an 8 mL glass vial was loaded with 6 mL of a DMA/H_2O mixture (2:1 v/v), a solution of H$_4$**L** in DMA (200 µL, 0.25 M), and an aqueous solution of $Cd(NO_3)_2{\cdot}4H_2O$ (400 µL, 0.25 M). The mixture was sonicated for a few minutes and then heated to 120 °C for 24 h. The mixture was then cooled to room temperature at a rate of 10 °C/h. Two different morphologies of colorless crystals were isolated and structurally characterized as compounds **2** and **3**.

Author Contributions: Conceptualisation: MCA, RPD, EP, MA. Data curation: MCA, EP, RPD, MA, SJC, JBO, GE. Investigation: MCA, EP, RPD, MA, SJC, JBO, GE, AP. Writing (original draft): MCA, RD, EP. Writing (reviewing ad editing): all authors. Funding acquisition: CC, LP. Validation: all authors.

Acknowledgments

The authors kindly acknowledge CINECA for the computational resources on the Galileo 100 supercomputer accessed within the ISCRA project BIFluoex, Fondazione di Sardegna for financial support, CeSAR for PXRD facilities, and Daniele Mele for TOC artwork.

Conflicts of interest

There are no conflicts to declare.

Notes and references

‡ Structural characterization data and selected bond lengths and angles are reported in ESI.

§ A solvent mask was calculated, and 250 electrons were found in a volume of 1220 Å^3 per unit cell. This is consistent with the presence of 24 H_2O molecules per unit cell.

1 B. Liu, W.-L. Yu, Y.-H. Lai, W. Huang, *Chem. Mater*., 2001, **13**, 1984–1991.
2 X. Guo, M. Baumgarten, K. Müllen, *Prog. Polym. Sci*., 2013, **38**, 1832–1908.
3 M. Leclerc, *J. Polym. Sci. Part A Polym. Chem*., 2001, **39**, 2867–2873.
4 U. Scherf and E. J. W. List, *Adv. Mater*., 2002, **14**, 477–487.
5 W. L. Yu, J. Pei, W. Huang, A. J. Heeger, *Adv. Mater*., 2000, **12**, 828–831.
6 X. Gong, P. K. Iyer, D. Moses, G. C. Bazan, A. J. Heeger,S. S. Xiao, *Adv. Funct. Mater.,* 2003, **13**, 325–330.
7 D. Wang, M. V. Ivanov, D. Kokkin, J. Loman, J.-Z. Cai, S. A. Reid, R. Rathore, *Angew. Chem. Int. Ed*., 2018, **57**, 8189–8193.
8 R. Rathore, S. H. Abdelwahed and I. A. Guzei, *J. Am. Chem. Soc*., 2003, **125**, 8712–8713.
9 D. Kokkin, M. Ivanov, J. Loman, J. Z. Cai, B. Uhler, N. Reilly, R. Rathore, S. A. Reid, *J. Chem. Phys*., 2018, **149**, 13431.
10 H. Qi, J. Chang, S. H. Abdelwahed, K. Thakur, R. Rathore, A. J. Bard, *J. Am. Chem. Soc*., 2012, **134**, 16265–16274.
11 B. Uhler, M. V. Ivanov, D. Kokkin, N. Reilly, R. Rathore, S. A. Reid, *J. Phys. Chem. C*, 2017, **121**, 15580–15588.

12 C. Poriel, C. Quinton, F. Lucas, J. Rault-Berthelot, Z. Jiang, O. Jeannin, *Adv. Funct. Mater*., 2021, **31**, 2104980
13 X. Duan, R. Lv, Z. Shi, C. Wang, H. Li, J. Ge, Z. Ji, Y. Yang, B. Li, G. Qian, *J. Solid State Chem*., 2019, **277**, 159–162.
14 X. Duan, Q. Zhang, J. Cai, Y. Cui, C. Wu, Y. Yang, G. Qian, *Microporous Mesoporous Mater*., 2014, **190**, 32–37.
15 H. J. Park, J. K. Jang, S. Y. Kim, J. W. Ha, D. Moon, I. N. Kang, Y.-S. Bae, S. Kim, D. H. Hwang, *Inorg. Chem*., 2017, **56**, 12098–12101.
16 P. Wang, J. Xu, Q. D. Zhuo, Y. S. Ma, H. J. Cheng, X. Y. Tang and R. X. Yuan, *Inorg. Chem. Commun*., 2016, **67**, 14–16.
17 J. P. Ma, Y. Yu and Y. Bin Dong, *Chem. Commun*., 2012, **48**, 2946–2948.
18 Y. Hong, S. Sun, Q. Sun, E.-Q. Gao, M. Ye, *Mater. Chem. Phys*., 2020, **243**, 122601.
19 Z. You, H. Li, L. Zhang, B. Yu, J. Zhang, X. Wu, *J. Phys. Chem. C*, 2017, **121**, 23072–23079.
20 F. Moreau, N. Audebrand, C. Poriel, *CrystEngComm* 2019, **22**, 293–303
21 H. D. Guo, X. M. Guo, S. R. Batten, J. F. Song, S. Y. Song, S. Dang, G. L. Zheng, J. K. Tang, H. J. Zhang, *Cryst. Growth Des.* 2009, **9**, 1394–1401.
22 L. C. Delmas, A. J. P. White, D. Pugh, A. Evans, M. A. Isbell, J. Y. Y. Heng, P. D. Lickiss, R. P. Davies, *Chem. Commun*., 2020, **56**, 7905–7908.
23 L. C. Delmas, P. N. Horton, A. J. P. White, S. J. Coles, P. D. Lickiss, R. P. Davies, *Chem. Commun*., 2017, **53**, 12524–12527.
24 A. Schoedel, M. Li, D. Li, M. O'Keeffe, O. M. Yaghi, *Chem. Rev.*, 2016, **116**, 12466−12535.
25 S. Su, C. Qin, Z. Guo, H. Guo, S. Song, R. Deng, F. Cao, S. Wang, G. Li, H. Zhang, *CrystEngComm*, 2011, **13**, 2935–2941.
26 R. O. Jones, *Rev. Mod. Phys.*, 2015, **87**, 897–923.
27 C. Adamo, V. Barone, *J. Chem. Phys*., 1999, **110**, 6158–6170.
28 F. Weigend, R. Ahlrichs *Phys. Chem. Chem. Phys*., 2005, **7**, 3297.
29 J. Tomasi, B. Mennucci, R. Cammi, *Chem. Rev*., 2005, **105**, 2999–3094.
30 R. L. Martin, "*J. Chem. Phys*., 2003, **118**, 4775–4777.
31 M. Kascha, *Discuss. Faraday Soc*., 1950, **9**, 14–19.
32 CrysAlisPro Software System, Rigaku Oxford Diffraction, (2020).
33 G. M. Sheldrick *Acta Crystallogr. Sect. A Found. Crystallogr.,* 2015, **71**, 3–8.
34 O. V. Dolomanov, L. J. Bourhis, R. J. Gildea, J. A. K. Howard, H. Puschmann *J. Appl. Crystallogr.*, 2009, **42**, 339–341.
35 G. M. Sheldrick *Sect. C Struct. Chem.*, 2015, **71**, 3–8.
36 M. J. Frisch, G. W. Trucks, H. B. Schlegel, G. E. Scuseria, M. A. Robb, J. R. Cheeseman, G. Scalmani, V. Barone, G. A. Petersson, H. Nakatsuji, X. Li, M. Caricato, A. V. Marenich, J. Bloino, B. G. Janesko, R. Gomperts, B. Mennucci, H. P. Hratchian, J. V. Ortiz, A. F. Izmaylov, J. L. Sonnenberg, D. Williams-Young, F. Ding, F. Lipparini, F. Egidi, J. Goings, B. Peng, A. Petrone, T. Henderson, D. Ranasinghe, V. G. Zakrzewski, J. Gao, N. Rega, G. Zheng, W. Liang, M. Hada, M. Ehara, K. Toyota, R. Fukuda, J. Hasegawa, M. Ishida, T. Nakajima, Y. Honda, O. Kitao, H. Nakai, T. Vreven, K. Throssell, J. A. Jr. Montgomery, J. E. Peralta, F. Ogliaro, M. J. Bearpark, J. J. Heyd, E. N. Brothers, K. N. Kudin, V. N. Staroverov, T. A. Keith, R. Kobayashi, J. Normand, K. Raghavachari, A. P. Rendell, J. C. Burant, S. S. Iyengar, J. Tomasi, M. Cossi, J. M. Millam, M. Klene, C. Adamo, R. Cammi, J. W. Ochterski, R. L. Martin, K. Morokuma, O. Farkas, J. B. Foresman, D. J. Fox, Gaussian 16, Revision C.01; Gaussian, Inc.: Wallingford CT, 2016
37 (a) R. Krishnan, J. S. Binkley, R. Seeger, J. A. Pople *J. Chem. Phys*., 1980, **72**, 650–654; (b) T. Clark, J. Chandrasekhar, G. W. Spitznagel, P. Von Ragué Schleyer *J. Comput. Chem*., 1983, **4**, 294–301; (c) M. J. Frisch, J. A. Pople, J. S. Binkley *J. Chem. Phys.,* 1984, **80**, 3265–3269.
38 A. Schäfer, H. Horn, R. Ahlrichs *J. Chem. Phys.*, 1992, **97**, 2571–2577.
39 F. Weigend, *Phys. Chem. Chem. Phys*., 2006, **8**, 1057–1065.
40 Y. Takeshi, P. D. Tew, N. C. Handy, *Chem. Phys. Lett.*, 2004, **393**, 51–57.
41 Y. Tawada, T. Tsuneda, S. Yanagisawa, *J. Chem. Phys*., 2004, **120**, 8425–8433.
42 A. E. Reed, R. B. Weinstock, F. Weinhold *J. Chem. Phys.*, 1985, **83**, 735–746.
43 D. Jacquemin, E. A. Perpète, G. Scalmani, M. J. Frisch, I. Ciofini, C. Adamo, *Chem. Phys. Lett*., 2006, **421**, 272–276.
44 D. Jacquemin, C. Adamo *Chem. Soc. Rev.*, 2012, **42**, 845–856.
45 G. Schaftenaar, J. H. Noordik *J. Comput. – Aided Mol. Des*., 2000, **14**, 123–134.
46 R. Dennington, T. A. Keith, J. M. Millam, GaussView, Version 6; Semichem Inc.: Shawnee Mission, KS, 2016.
47 Chemissian v. 4.67, a computer program to analyze and visualize quantum-chemical calculations written by L. Skripnikov. For the current version, see http://www.chemissian.com.

View Article Online DOI: 10.1039/D2CE01552H